



Experimental and density functional theory study of the Li⁺ desorption in spinel/layered lithium manganese oxide nanocomposites using HCl

Ruth Pulido^{a,b,*}, Nelson Naveas^{a,b}, Raúl J. Martín-Palma^a, Teófilo Graber^b, Iván Brito^c, Jacobo Hernández-Montelongo^d, Miguel Manso Silván^{a,e}

^a Departamento de Física Aplicada and Instituto Universitario de Ciencia de Materiales Nicolás Cabrera, Universidad Autónoma de Madrid, 28049 Madrid, Spain

^b Departamento de Ingeniería Química y Procesos de Minerales, Universidad de Antofagasta, Avenida Angamos 601, Antofagasta, Chile

^c Departamento de Química, Universidad de Antofagasta, Avda. Universidad de Antofagasta 02800, 1240000 Antofagasta, Chile

^d Departamento de Ciencias Matemáticas y Físicas, UC Temuco, 4813302 Temuco, Chile

^e Centro de Microanálisis de Materiales, Universidad Autónoma de Madrid, Campus de Cantoblanco, 28049 Madrid, Spain

ARTICLE INFO

Keywords:

Lithium desorption
Lithium manganese oxide
Li₂MnO₃
Lithium ion-sieves
Density functional theory
Nudged elastic band

ABSTRACT

The increasing demand for portable electronic devices and batteries has led to a growing interest in Li compounds. Lithium manganese oxides (LMO) are the most popular lithium-ion sieves (LIS) precursor materials due to their high lithium adsorption capacity and selectivity. The key step in forming LIS is the lithium desorption process from the crystalline lattice of the LMO. However, this process has been less researched than its counterpart, the lithium adsorption process. In this line, there are some studies describing the process of lithium desorption in acid media from spinel-type LMO. Nevertheless, there is no evidence of the lithium desorption process of layered-type lithium-rich LMO in acidic media. In the present work, we investigated the lithium desorption behavior of different LMO nanocomposites in HCl. LMOs with different Li/Mn ratios were synthesized by promoting the lithium-rich layered phase (Li₂MnO₃). The morphology, size, crystallinity, chemical composition, and surface properties of LMO nanocomposites and delithiated products were studied. In addition, density functional theory (DFT) calculations were carried out to understand the differential lithium desorption behavior, confirming its dependence on the Li/Mn ratio of the LMO nanocomposites. Herein, we demonstrate that the lithium diffusion energy barrier plays a major role during lithium desorption from LMO nanocomposites. Our results suggest that an exhaustive characterization of lithium precursor materials (LMO) is necessary to select a suitable desorption process.

1. Introduction

Lithium and derivative compounds in the form of ceramics or glasses play a key role in several commercial applications such as batteries, pharmaceuticals, and lubricants, having become strategic technological elements [1–3]. Today, there is a dramatic increase in global lithium consumption due to principally increased demand for electronic devices and electric vehicles [4]. In this context, the lithium extraction process has received great attention. Currently, the primary resources of lithium are brine deposits from South America (Chile, Bolivia, and Argentina), followed by hard rock resources [4,5]. Thus far, different methods for lithium extraction from brine have been explored, such as evaporative crystallization [6,7], solvent extraction [8–10], electrochemical

adsorption [11], membrane technology [12,13], and lithium ion-sieves (LIS) [14]. The most commonly used as the standard commercial process in the lithium industry is solar evaporation-precipitation technology [5]. However, major concerns with this technology are the lithium selectivity, long production time, low recovery efficiency, and the severe impact on ecosystems [7,15]. Although the membrane and electrochemical technologies have shown interesting results in terms of selectivity, these technologies are highly constrained by their operational conditions and costs [5]. For these reasons, active research is currently focusing on improving lithium selectivity, efficiency, and extraction rate, considering low capital cost and environmental impact. In this context, LIS technology has received increasing attention because it overcomes the issues mentioned above [14]. Thus, LIS technology

* Corresponding author at: Departamento de Física Aplicada and Instituto Universitario de Ciencia de Materiales Nicolás Cabrera, Universidad Autónoma de Madrid, 28049 Madrid, Spain.

E-mail address: ruth.pulido@estudiante.uam.es (R. Pulido).

<https://doi.org/10.1016/j.cej.2022.136019>

Received 2 February 2022; Received in revised form 21 March 2022; Accepted 23 March 2022

Available online 26 March 2022

1385-8947/© 2022 The Author(s). Published by Elsevier B.V. This is an open access article under the CC BY-NC-ND license (<http://creativecommons.org/licenses/by-nc-nd/4.0/>).

allows a high adsorption capacity, superior lithium selectivity, and environmentally friendly and feasible production along with highly pure and readily accessible lithium products [14,16–18].

The synthesis route of LIS starts with the synthesis of the precursor material. These materials can be synthesized using various synthetic routes, such as soft chemical synthesis methods (sol–gel, hydrothermal, and molten salts) and solid-state synthesis [19]. Whatever the synthesis is chosen, the next step is stripping lithium from the crystalline lattice of the precursor materials by acid treatment. Thus, the lithium stripping results in the formation of vacant crystal sites that act by steric-effect as lithium ion-sieves [14,20,21].

From the point of view of the metal transition framework, LIS can be obtained principally from two types of precursor materials, namely, lithium manganese oxide (LMO) and lithium titanium oxide (LTO). The most widely used precursor materials have been spinel-type lithium manganese oxide (LMO) due to their high lithium adsorption capacity, excellent regeneration performance, and simplified synthesis compared to LTO [21–23]. Different spinel-type LMO can be found depending on the Li/Mn ratio [24–26]. The chemical formula $\text{Li}_x\text{Mn}_{3-x}\text{O}_4$ ($0 \leq x \leq 1.33$) represents these spinel-type LMO. Their spacial ordering is based on the cubic crystalline structure of the $Fd3m$ space group represented by $(\text{Li})_{8a}[\text{Mn(III)Mn(IV)}]_{16d}\text{O}_4$ formula. In the spinel-type LMO, the Li^+ ions occupy the tetrahedral 8a sites, while the Mn (III) and Mn (IV) ions are randomly distributed over octahedral 16d sites with mole ratio 1:1 and O^{2-} ions occupy close-packed cubic 32e sites [27]. For Li/Mn ratio close to 2, layered-type LMO with the chemical formula Li_2MnO_3 can be obtained. Interestingly, a theoretical study proposed the lithium-rich layered-type LMO as promissory material for lithium recovery applications [28]. This precursor material is characterized by a monoclinic special ordering of space group $C2/m$ represented by $\{(\text{Li}_{1/2})_{2c}(\text{Li})_{4h}\}_{\text{interslab}}\{(\text{Li}_{1/2})_{2b}(\text{Mn})_{4g}(\text{O})_{4i}(\text{O}_2)_{8j}\}$ formula. The lithium-ion is distributed in octahedral sites into the $[\text{Li}^+]$ layer stack (2c and 4 h sites) and transition metal $[\text{LiMn}_2]$ layer (2b sites), while the Mn (IV) ions are distributed octahedral 4 g sites [29]. This material has a higher lithium theoretical adsorption capacity. Despite this, few studies have evaluated its performance as a precursor material of lithium adsorbents. Qianqian Yu *et al.*, applied a series of lithium-ion sieve precursor materials based on LMO composites with Li_2MnO_3 formation as a secondary phase [30]. They carried out a standard lithium desorption process (0.1 M HCl for 12 h) for all LMO composites. However, their result shows that the lithium desorption process occurs successfully in the spinel phase and not in the layered phase. They found that the lithium adsorption capacity decreased with increasing layered- Li_2MnO_3 in LMO composites. Other studies have reported a similar effect of the Li_2MnO_3 content on the adsorption performance of LMO [31,32]. Nevertheless, they did not explain the reasons or the underlying mechanism for this behavior. The optimization of the desorption process plays a crucial role in the LIS application. Some studies have shown interest in explaining the mechanism of lithium desorption in spinel-type LMO. In fact, different mechanisms have been proposed, such as the ion-exchange by topotactic extraction, redox reactions via disproportionation of Mn^{+3} to Mn^{+4} and Mn^{+2} , or both mechanisms [33–36]. Despite the great information available for spinel-type precursor materials, there is still a technological gap to optimize the desorption behavior in layered-type LMO as lithium adsorbent precursor material. Thus, a systematic comparative study of the desorption process of spinel-layered LMO composites in acidic media is proposed.

This report provides experimental and theoretical results about the lithium desorption process of LMO nanocomposite containing spinel and layered phase. First, we hydrothermally synthesized LMO nanocomposites consisting of spinel $\text{Li}_{1.12}\text{Mn}_{1.7}\text{O}_4$ ($Fd3m$) and layered Li_2MnO_3 ($c2/m$). By controlling the increase of the lithium-rich monoclinic phase, we formed LMO nanocomposites with different Li/Mn ratios. Then, the LMO nanocomposites were systematically submitted to the lithium desorption process at different HCl concentrations and temperatures. A full characterization of the LMO and their delithiated

nanocomposites in terms of morphology, size, crystallinity, chemical composition, and physical properties were performed. Also, crystalline ground state structures, electronic properties, and their intrinsic lithium diffusion pathways were investigated by Density Functional Theory (DFT) calculations for pure phases of $\text{Li}_{1.12}\text{Mn}_{1.7}\text{O}_4$ ($Fd3m$) and Li_2MnO_3 ($c2/m$) along with their delithiated structures.

2. Materials and methods

2.1. Chemicals

All the chemicals and standards used in this works are of analytical grade (purity > 98%). Salts of LiOH and MnSO_4 , acquired from Merck Milipore®, were used for the synthesis of LMO nanocomposites. Hydrogen peroxide (H_2O_2 , 30%) and hydrochloric acid (HCl, 37%) were acquired from Sigma–Aldrich.

2.2. Synthesis of LMO nanocomposites materials

LMOs nanocomposites materials were synthesized by a hydrothermal method using a previously reported protocol [37]. The crystallization temperature was varied from 110 °C to 170 °C, denoting samples as LMO-110, LMO-140, and LMO-170. Spinel-type LMO in pure phase (LMO-s) was synthesized in similar conditions (3 mol·L^{−1} LiOH, 1.2 mol·L^{−1} H_2O_2 and 0.4 mol·L^{−1} MnSO_4) at 110 °C. The resulting materials were centrifugated and washed several times with ultrapure water. The precipitate was dried and calcined at 400 °C for 4 h.

2.3. Desorption of LMO nanocomposites

The behavior of the lithium desorption along to manganese dissolution of the nanocomposites was studied in a batch system. In order to evaluate the lithium desorption rate, 50 mg of LMO were dispersed in 50 ml of 0.1, 0.25 and 0.5 M HCl and stirred for 72 h at 25, 40 and 60 °C. Aliquots of 1 ml were sampled at different intervals of time (0.25–72 h). The resulting material (now named HMO) was centrifugated and filtered through an Acrodisc® 13 mm syringe filter with 0.2 µm Supor® membrane (Pall Life Sciences, Ann Arbor, USA). The sample compositions were determined using inductively coupled plasma optical emission spectroscopy (ICP-OES, Perkin Elmer Optima 2100 DV). The desorption capacity values (q) were calculated from the change of solution concentration using the following equation:

$$q = \frac{(C_e - C_0) \times V}{m \times q_e} \times 100\%$$

where q_e lithium or manganese contents (mg/g) and C_0 and C_e are the initial and final concentrations (mg/L), respectively, V is the volume of solution (L) and m is the mass of adsorbent (g).

2.4. Characterization techniques

The crystallographic structure of the LMO nanocomposites and their delithiated phases were examined using powder X-ray Diffraction (XRD) in a Bruker New D8 Advance X-ray diffractometer equipped with a Johansson monochromator (Cu-Kα1 radiation, $\lambda = 1.5406$ Å) and LYNXEYE XE detector. The diffraction patterns were scanned from 2θ 10° to 90°, with an angular step of 0.02° and 2°/s. The diffraction data have been refined through the Rietveld technique using the Match software (Crystal Impact).

Morphological characterization of LMO nanocomposites and their delithiated phases have been studied by field-emission scanning electron microscopy (FESEM; Philips XL-40FEG), operating with an acceleration potential of 10 keV. The morphology and microstructure were further investigated using high-resolution transmission electron microscopy (HR-TEM) and electron diffraction (ED), with a JEOL 2100F, operating at an accelerating voltage of 200 kV.

Fourier transform infrared (FT-IR) spectroscopy was used to identify

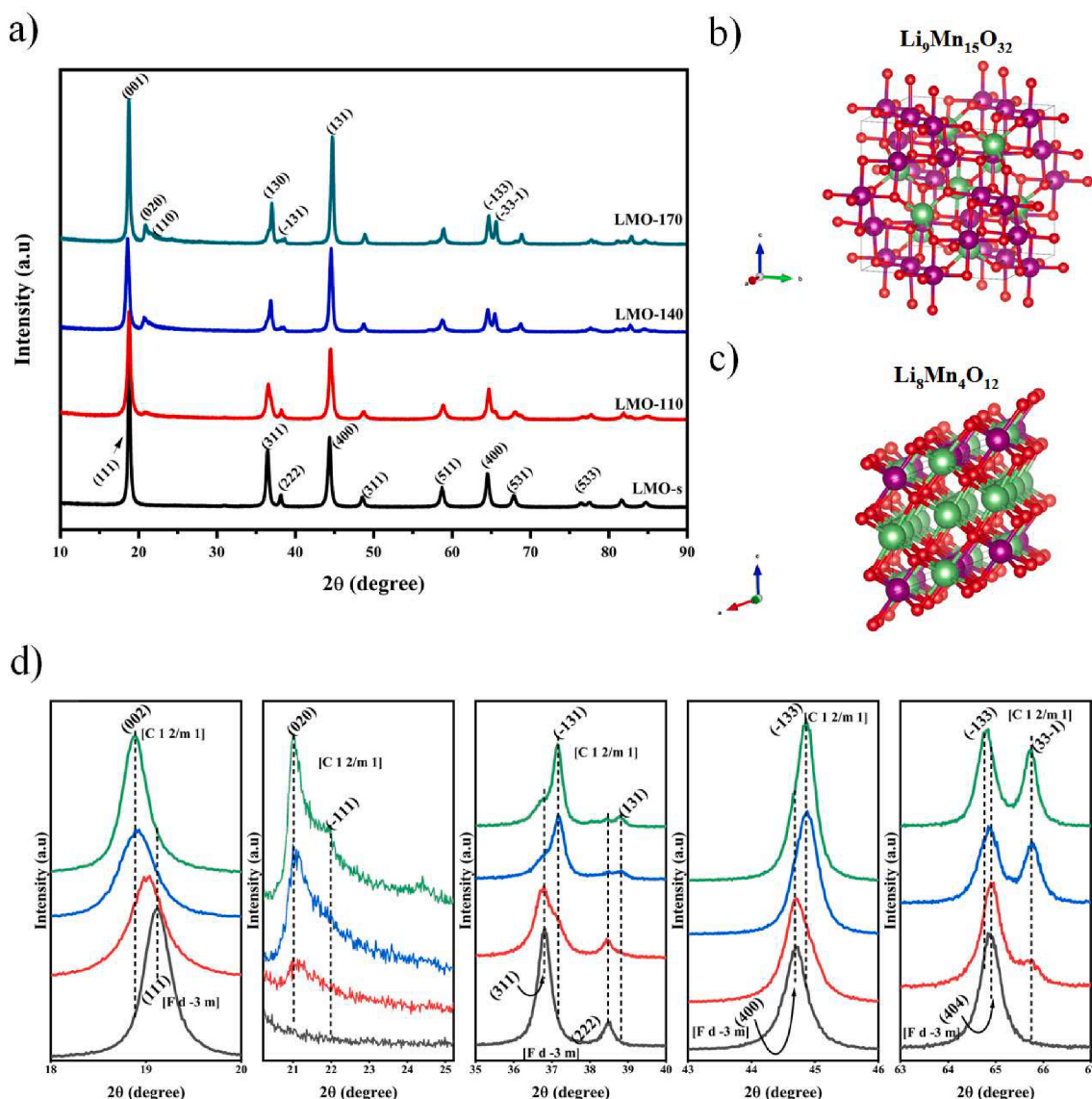


Fig. 1. XRD patterns of the synthesized LMO nanocomposites (a), crystal structure of the cubic spinel $\text{Li}_{1.12}\text{Mn}_{1.7}\text{O}_4$ (b), crystal structure of the layer-structured monoclinic Li_2MnO_3 (c) and detailed changes in XRD patterns at different 2θ (degree) for samples: LMO-s (black), LMO-110 (red), LMO-140 (blue) and LMO-170 (green) (d).

the functional groups in the LMO nanocomposites and their delithiated phases. The FT-IR spectra were obtained using a Spectrum Two FT-IR Spectrometer in the $4000\text{--}450\text{ cm}^{-1}$ range with 4 cm^{-1} resolution and far-infrared in the $200\text{--}350\text{ cm}^{-1}$ range with 2 cm^{-1} resolution.

The specific surface areas of the LMO nanocomposites and their delithiated phase were calculated using the multiple-point Brunauer–Emmett–Teller (BET) method using an ASAP2010 instrument (Micromeritics). The sample compositions were determined using inductively coupled plasma optical emission spectroscopy (ICP-OES, Perkin Elmer Optima 2100 DV) after the samples digestion in a mixture of HCl ($2\text{ mol}\cdot\text{L}^{-1}$) and HNO_3 ($2\text{ mol}\cdot\text{L}^{-1}$) in the volume ratio 1:1. The Mn average oxidation state (AOS) of the LMO nanocomposites was determined using a two-step colorimetric method based on Leucoberbelin I and formaldoxime methods (20).

2.5. DFT calculations

DFT calculations were performed to obtain the optimized cell parameters and electronic properties for $\text{Li}_{1.12}\text{Mn}_{1.7}\text{O}_4$ and Li_2MnO_3 and their delithiated structures using the Quantum ESPRESSO 6.5

computational package [38]. The supercells used to represent $\text{Li}_{1.12}\text{Mn}_{1.7}\text{O}_4$ and Li_2MnO_3 were $\text{Li}_9\text{Mn}_{15}\text{O}_{32}$ and $\text{Li}_8\text{Mn}_4\text{O}_{12}$, respectively. In order to construct the delithiated structures of LMO, Li atoms were replaced by H atoms. Three delithiated structures, namely, $\text{Li}_8\text{H}_1\text{Mn}_{15}\text{O}_{32}$ (replacing Li at 16d position), $\text{H}_8\text{Li}_1\text{Mn}_{15}\text{O}_{32}$ (replacing all Li at 8a positions), and $\text{H}_9\text{Mn}_{15}\text{O}_{32}$ (fully delithiated), were constructed for $\text{Li}_9\text{Mn}_{15}\text{O}_{32}$. Likewise, three delithiated structures, namely, $\text{Li}_6\text{H}_2\text{Mn}_4\text{O}_{12}$ (replacing Li from $[\text{LiMn}_2]$ layer position), $\text{H}_6\text{Li}_2\text{Mn}_4\text{O}_{12}$ (replacing Li from $[\text{Li}]$ layer position), and $\text{H}_8\text{Mn}_4\text{O}_{12}$ (fully delithiated), were constructed for $\text{Li}_8\text{Mn}_4\text{O}_{12}$ supercells. Ultrasoft pseudopotentials were chosen for Li, Mn, O, and H. All calculations were performed with Generalized Gradient Approximation (GGA) and parameterized by Perdew, Burke, and Ernzerhof (PBE). Moreover, the strong correlation of the 3d transition metal was taken into account using the DFT + U method. The Hubbard U value was 3.5 for the $\text{Li}_{1.12}\text{Mn}_{1.7}\text{O}_4$ (mixture of $\text{Mn}^{+3}/\text{Mn}^{+4}$ ions) and 5.0 for the Li_2MnO_3 (Mn^{+4} ions). The kinetic energy cutoffs for wavefunction was set to 40 Ry for all calculations. The convergence criteria for the energy tolerance was set to 10^{-6} Ry, and the force tolerance was set to 10^{-3} Ry per Bohr. The Monkhorst-Pack method [39] was used to sample the k-point mesh with $3 \times 3 \times 3$ for

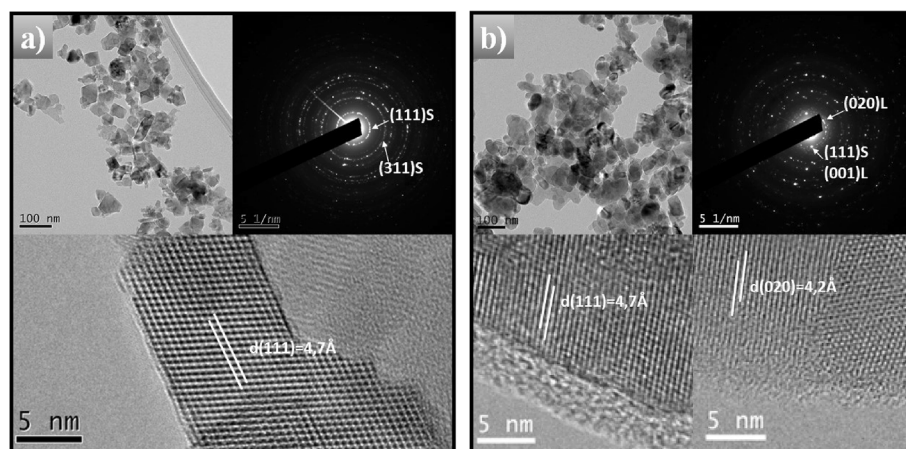


Fig. 2. TEM and HRTEM images and their corresponding SAED patterns of LMO-s (a) and LMO-170 (b).

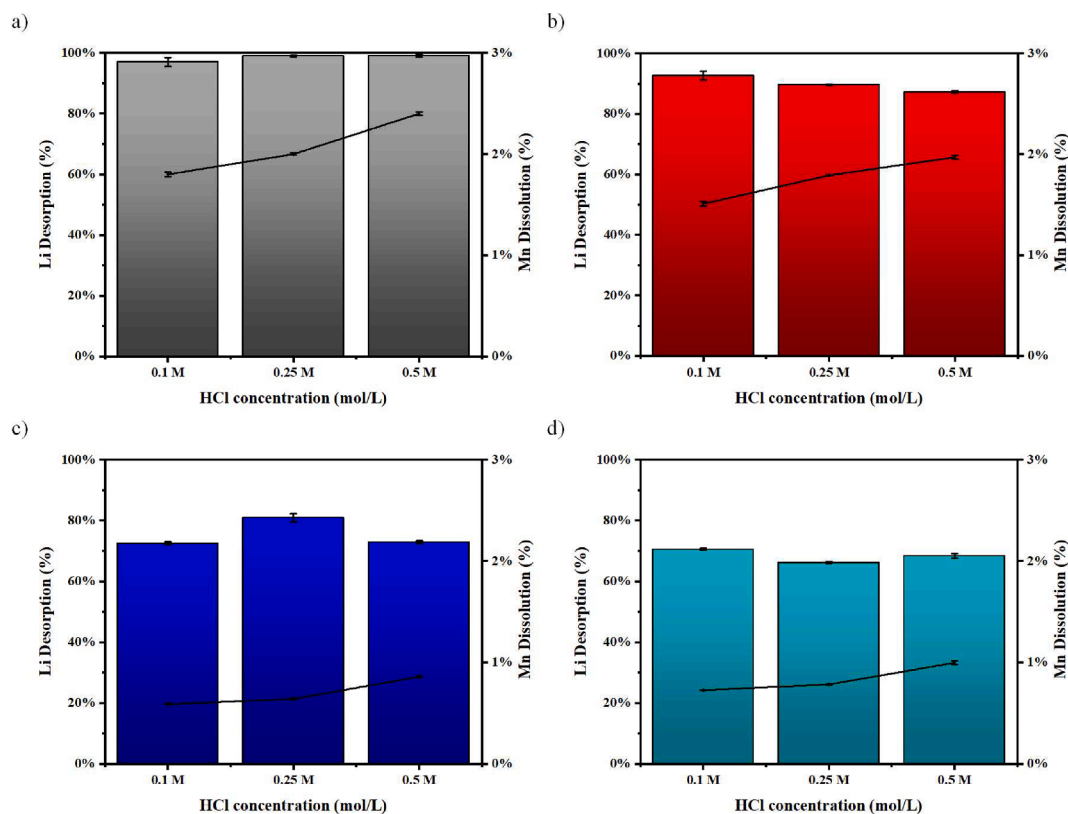


Fig. 3. Acid delithiation treatment at 0.1 M, 0.25 M and 0.5 M HCl for LMO-s (a), LMO-110 (b), LMO-140 (c) and LMO-170 (d). (Li desorption (%): column, Mn dissolution (%): line).

$\text{Li}_{1.12}\text{Mn}_{1.7}\text{O}_4$ and $6 \times 6 \times 6$ for Li_2MnO_3 . All calculations were carried out considering spin polarization and ferromagnetic ordering. The obtained optimized cell parameters and atomic positions for $\text{Li}_9\text{Mn}_{15}\text{O}_{32}$, $\text{Li}_8\text{Mn}_4\text{O}_{12}$, and their delithiated structures were used to construct the simulated XRD spectra using the VESTA software package [40].

Nudged Elastic Band (NEB) method implemented by Quantum ESPRESSO 6.5 computational package was employed to obtain the minimum-energy pathways for Li-ion diffusion. All NEB calculations were performed using nine images and a path convergence threshold of 0.05 eV Å⁻¹. Grimme's DFT-D was adopted as the long-range dispersion correction.

3. Results and discussion

3.1. LMO nanocomposites characterization

LMO precursor materials with a different Li/Mn ratio were successfully synthesized by the hydrothermal method, favoring the lithium-rich layered monoclinic phase (Li_2MnO_3). The obtained LMO nanocomposites were characterized in terms of crystallinity, chemical composition, morphology, size, and surface properties.

In order to determine the crystalline structure of the synthesized LMO nanocomposites, XRD spectra were analyzed. Fig. 1(a-c) shows the characteristic XRD patterns of the different LMO nanocomposites and their crystalline structures. Two phases can be evidenced (Fig. 1a). The

Table 1

Chemical analysis of the LMO nanocomposites after HCl treatment at different concentrations.

Nanocomposite	HCl Concentration	Li/Mn ratio	Mn AOS
LMO-s	–	0.65	3.46
	0.1	0.02	3.68
	0.25	0.00	3.70
	0.5	0.00	3.69
LMO-110	–	1.07	3.65
	0.1	0.08	3.79
	0.25	0.07	3.82
	0.5	0.07	3.82
LMO-140	–	1.72	3.88
	0.1	0.35	3.90
	0.25	0.28	3.91
	0.5	0.36	3.91
LMO-170	–	1.76	3.91
	0.1	0.48	3.92
	0.25	0.47	3.93
	0.5	0.46	3.92

relative diffraction intensities corresponding to (111), (311), (222), (400) and (404) confirmed the formation of the cubic spinel $\text{Li}_{1.12}\text{Mn}_{1.7}\text{O}_4$ ($Fd3m$ spatial group; COD entry # 96-151-3976), while characteristic peaks of monoclinic Li_2MnO_3 ($c2/m$ spatial group; COD entry # 96-154-4474) at (001), (020) and (33-1) planes were found. In order to obtain detailed information about the spinel/layered ratio of LMO nanocomposites, we carried out phase quantification by Rietveld

refinement method. Rietveld refinement method allows to model a full powder diffraction profile based on crystal structure data, specimen and instrument effects, by fitting a vast range of corresponding functions parameters. In order to find the minimum difference between the calculated and the experimental powder diffraction pattern, the parameters are varied by applying a nonlinear least-squares technique [41]. Thus, by using the previously determined LMO phases, the quantification by Rietveld refinement results in 100% spinel phase for LMO-s sample, 70.7% spinel and 29.3% layered phase for the LMO-110 sample, 15.6% spinel and 84.4% layered phase for the LMO-140 sample and 13.2% spinel and 86.8% layered phase for LMO-170 sample (Fig. S1). The cell parameters obtained from the Rietveld refinement of the LMO phases in the nanocomposites are presented in Table S1. Fig. 1d shows the main differences between the diffraction patterns of our nanocomposites in the ranges 18–20°, 20–25°, 35–40°, 38–46°, and 63–67°. The absence of any peak related to the layered phase in the LMO-s sample is noticeable. In contrast, the increase of the layered phase in the LMO-110, LMO-140 and LMO-170 samples is observed. In this context, shoulder-like peaks between 20 and 25° correspond to (020) and (110) planes, and peak splitting between 63 and 67°, assigned to (–133) and (33–1) planes are attributed to the superlattice in Li_2MnO_3 [42,43]. These results are according to the chemical content of our nanocomposites, where both the Li/Mn ratio and the Mn AOS of the LMO nanocomposites increased with increasing layered phase (see Table S2).

The morphological study of the different nanocomposites was

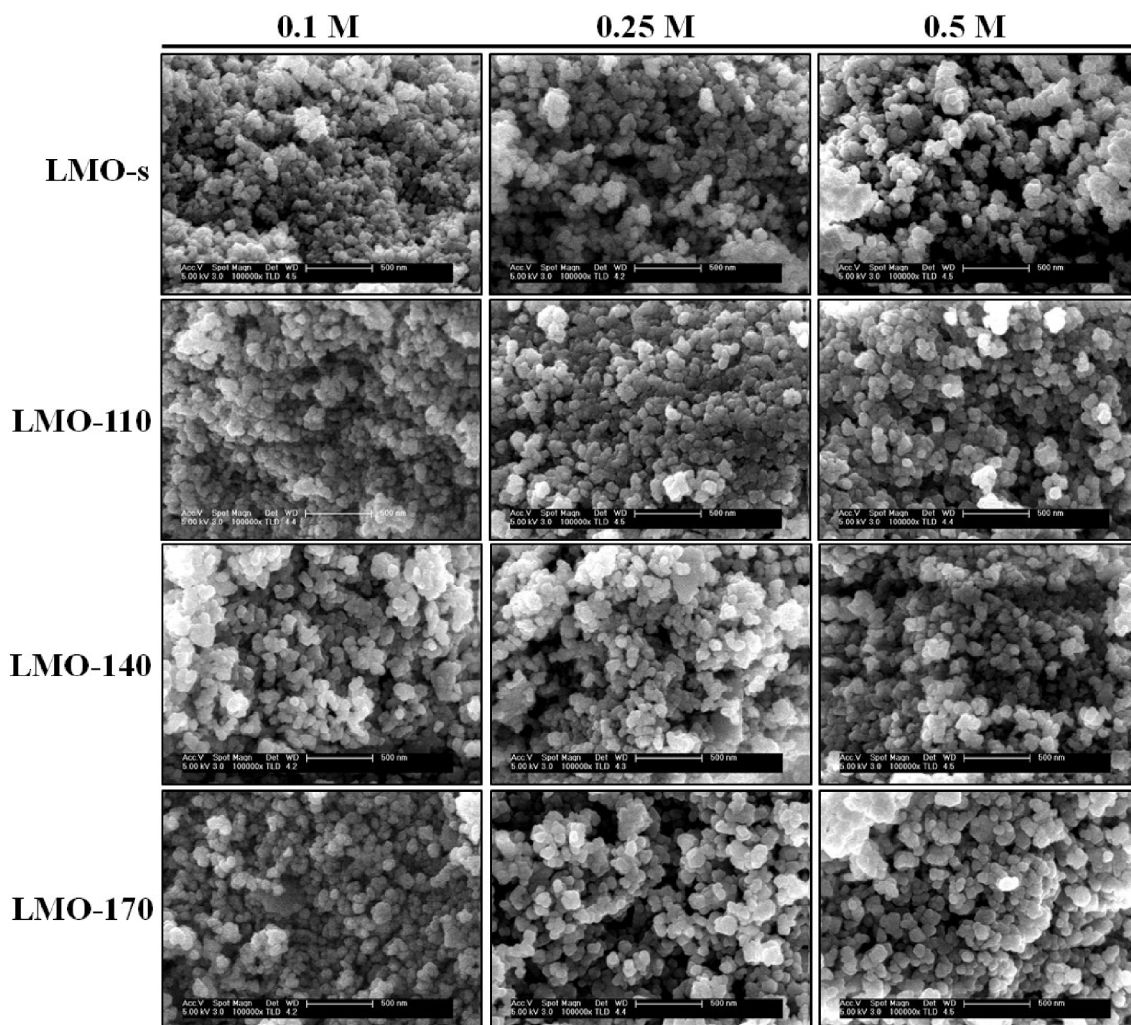


Fig. 4. FESEM images of the LMO nanocomposites after the treatment with HCl at different concentrations.

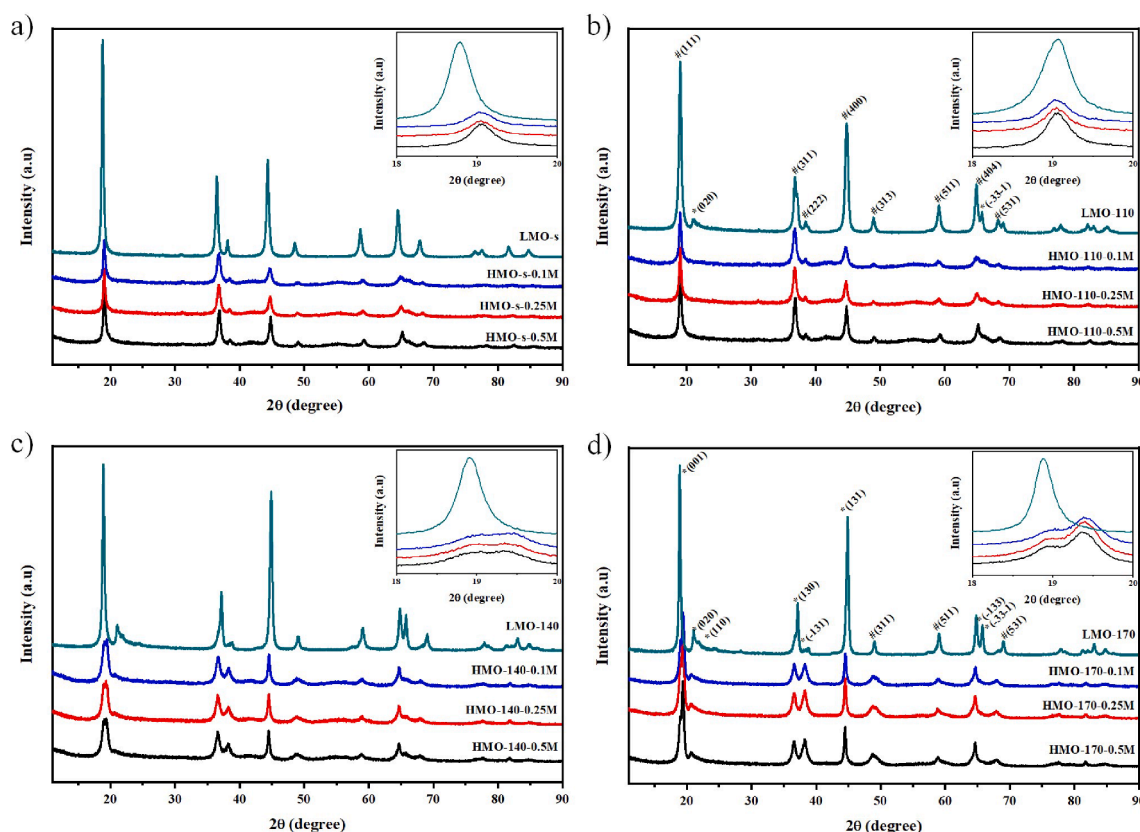


Fig. 5. Comparison of the XRD patterns for LMO and their delithiated HMO at different HCl concentrations. HMO-s (a), HMO-110 (b), HMO-140 (c) and HMO-170 (d). # spinel and *layered.

performed by FESEM. Fig. S2 shows FESEM images of the synthesized LMO nanocomposites. The results indicate that all samples exhibit agglomerated nanoparticles. In particular, it is observed that the nanocomposites with a low Li/Mn ratio (LMOs and LMO 110 samples) exhibit nanostructured nature with mixed granular and cubic morphologies (Fig. S2a-b). Meanwhile, at a high Li/Mn ratio (LMO-140 and LMO 170 samples), the distribution of nanoparticles results in a mixture of granules and nanorod morphologies (Fig. S2c-d). The mean nanoparticle size estimated from FESEM images for the LMOs, LMO-110, LMO-140, and LMO-170 nanocomposites was found to be 26 ± 6 nm, 27 ± 4 nm, 37 ± 5 nm, and 44 ± 7 nm, respectively.

TEM and HRTEM were subsequently used to study the microcrystallinity and local microstructure of the most representative samples at low and high Li/Mn ratios. Fig. 2 shows TEM and HRTEM images and their corresponding SAED patterns of LMO-s (a) and LMO-170 (b). TEM images reveal that both LMO-s and LMO-170 samples present agglomerated nanoparticles with cubic and granular morphologies. The LMO-s sample has particle sizes between 10 and 50 nm, while the LMO-170 sample confirms the presence of nanocubes of about 25–60 nm. The local study of the microstructure in the samples with low Li/Mn ratio (LMO-s sample) showed the presence of a single spinel-phase oriented along (111) and (311) zone axes. On the contrary, the samples with a high Li/Mn ratio (LMO-170 sample) exhibit nanoparticles with both spinel and layered phases oriented along the [111] and [020] zone axes, respectively.

3.2. Li^+ desorption process behavior at different HCl concentrations

Once the physicochemical characterization of the precursor material was performed, we studied the desorption process of the different LMO nanocomposites. Fig. 3 shows the effect of the different acid treatments on the LMO nanocomposites. First, it is important to note that at 24 h of

the incubation with HCl at room temperature, the delithiated process in the pure spinel phase (LMO-s) is complete [16,44]. On the contrary, samples with the presence of the layered phase (LMO-110, LMO-140, and LMO-170) did not fully delithiate their structures after the desorption process [30]. More interestingly, these LMO samples exhibited a differential delithiation behavior depending on the layered phase content. According to the lithium-rich phase increase, the percentage of lithium desorption decreases from 100 to 70%. Remarkably, the increment of the HCl concentration has no significant effect on the lithium desorption performance (Fig. 3.b); therefore, the increase from 0.1 to 0.5 M HCl does not trigger a rise in lithium desorption. In this context, the lithium desorption process in spinel-type LMO using both 0.1 M and 0.5 M HCl with the same acid incubation time has been reported successful [16,44,45]. However, in potassium-doped spinel structures, it has been shown that varying the HCl concentration in the range from 0.3 to 1.2 M has a differential effect on lithium desorption [46]. On the other hand, our results showed that the rise of the lithium-rich layered phase induces a decrease in manganese dissolution from 1.7% to 0.7%. Although reported and own research have shown that the lithium desorption process can be effective independently of the acid concentration, an important issue concerning manganese dissolution is evidenced with increasing HCl concentration. Thus, Xiao *et al.* reported dissolution of 2% Mn at 0.5 M HCl, while Qian *et al.*, 5.43% at 0.6 M HCl [45,47]. Therefore, the proper selection of the acid concentration is essential to avoid destabilizing the LMO structure via manganese dissolution [14].

In order to obtain the whole picture, we realized a study of the chemical content for all solid samples (see Table 1). After the lithium desorption process, all samples showed that Li/Mn ratio decreased. Remarkably, the Mn AOS increases for delithiated LMO-s and LMO-110 samples, probably due to the redox reaction between Mn^{+3} and Mn^{+4} [48]. In contrast, with the increased layered phase, the Mn AOS does not

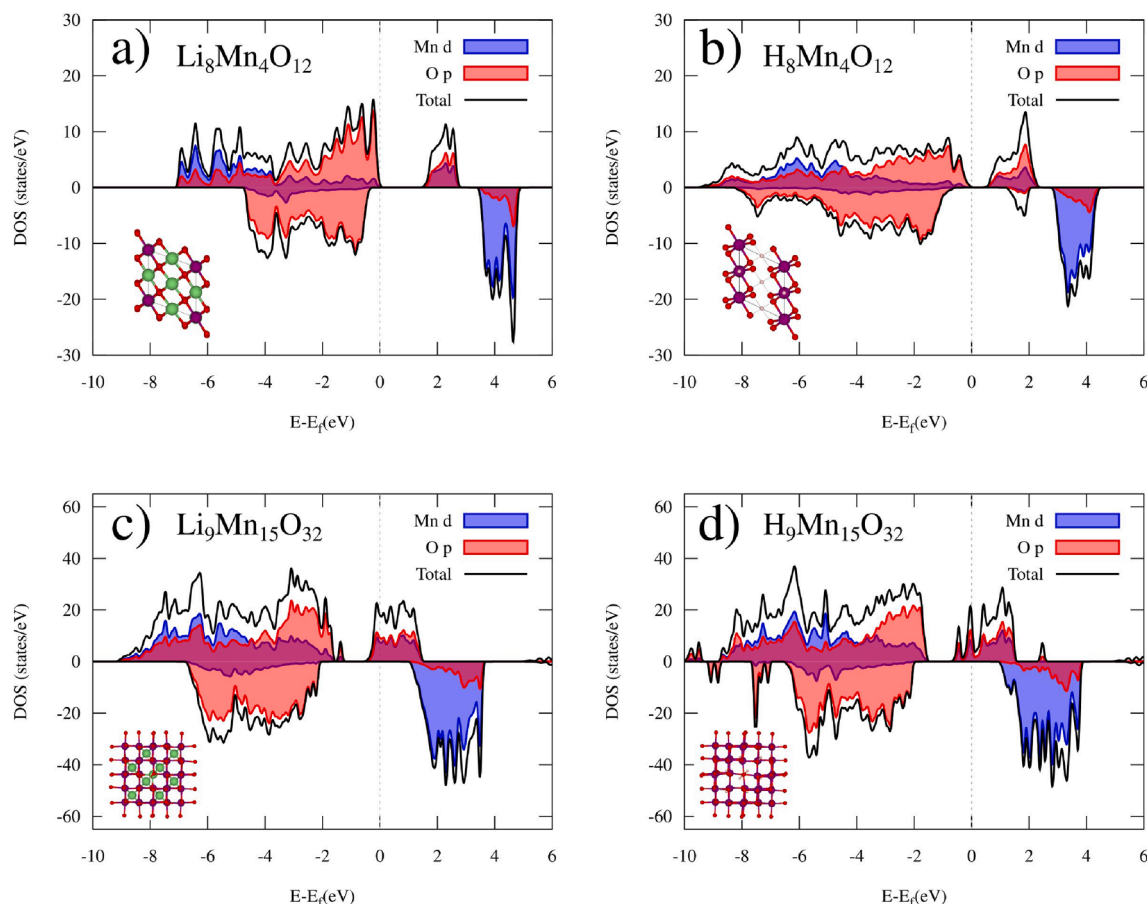


Fig. 6. Density of states for the ground state structure of Li_2MnO_3 and $\text{Li}_{1.12}\text{Mn}_{1.7}\text{O}_4$: fully lithiated structures ($\text{Li}_8\text{Mn}_4\text{O}_{12}$ (a) and (c) $\text{Li}_9\text{Mn}_{15}\text{O}_{32}$ supercells) and delithiated structures ($\text{H}_8\text{Mn}_4\text{O}_{12}$ (b): and (d) $\text{H}_9\text{Mn}_{15}\text{O}_{32}$ supercells), respectively.

change significantly for LMO-140 and LMO-170 samples, indicating that the redox reaction does not take place during the lithium desorption process [49,50].

Interestingly, FESEM analysis showed that the crystal size increased in all samples with increasing acid concentration (Fig. 4). All samples exhibit agglomerated nanoparticles with spheric morphologies. In particular, it is observed that the LMO-s crystal size increased from 51 ± 6 nm at 0.1 M to 57 ± 7 nm at 0.5 M HCl, the LMO-110 from 54 ± 6 nm at 0.1 M to 59 ± 6 nm at 0.5 M HCl. LMO-140 from 45 ± 3 nm at 0.1 M to 56 ± 6 nm at 0.5 M HCl and LMO-170 from 58 ± 5 nm at 0.1 M to 78 ± 9 nm at 0.5 M HCl. The specific surface area analysis for LMO nanocomposites delithiated with 0.5 M HCl was also studied by BET assays. Experimental BET values were found to be 68.6 ± 0.2 m²/g for HMO-s, 70.3 ± 0.2 m²/g for HMO-110, 63.6 ± 0.2 m²/g for HMO-140, and 46 ± 0.2 m²/g for HMO-170. Therefore, there is an increase in specific surface area after the desorption process compared to the lithiated LMO. These results agree with other studies that reported an increase of the specific surface area with lithium desorption [35,51].

In order to evaluate the evolution of the crystalline structure of LMO nanocomposites after acid treatment, we performed XRD analysis. Fig. 5 shows the experimental XRD spectra of LMO and HMO for each nanocomposite series at different HCl concentrations. In general, the experimental results reveal that increasing the HCl concentration has no differential effect on the crystallinity of nanocomposites of the same series. Nevertheless, the diffraction intensity decreases in all samples after the desorption process. Likewise, the main diffraction indices shifted to higher angles after acid treatment, suggesting that crystalline interplanar spacing decreased. This change has been attributed to the Li^+ deintercalation from the crystalline lattice of LMO [17,46,52]. More interestingly, we have recently reported that depending on the content

of the LMO phase, the desorption process exhibits a differential effect on the HMO structure [37]. In this sense, the XRD pattern of HMO-s and HMO-110 samples shows that the main diffraction indices of the LMOs and LMO-110 samples ((111), (311), (400) and (404)) are preserved after the desorption process (Fig. 5 a,b). Thus, both HMO-s and HMO-110 samples have a well-defined cubic-spinel crystal structure [36,51]. Curiously, there is no evidence of any diffraction indices of the C2/m space group in the HMO-110 sample, suggesting a structural transformation from layered to spinel phase [53–55]. On the other hand, the HMO-140 and HMO-170 samples show the (020) diffraction index and the double peaks around 37° 2θ angles corresponding to the (311) and (130) planes index to C2/m space group [56]. Diffraction indices corresponding to the spinel phase ((313), (511), and (531)) are also detected (Fig. 5 c,b). Based on these results, we conclude that the HMO-140 and HMO-170 samples exhibit a mixture of spinel and layered phases. In this line, Chitrakar *et al.* [57] reported that the crystalline structure in monoclinic-type precursor materials is conserved during the lithium desorption process. However, based on XRD simulation, this adsorbent was indexed as layered double hydroxide type with the $3R_1$ sequence of oxygen layers ($[(\text{OH})_2\text{OTi}_2(\text{OH})_2]$) by Cheng *et al.* [58].

In order to elucidate and grasp a better understanding of the structural transformation of our nanocomposites after the desorption process, quantum mechanics-based first-principle calculations were conducted. First, the structural parameters of the relaxed computational cell for the different lithiated and delithiated states in pure-phase LMOs were calculated by the GGA + U method (Table S3, S4). Also, the optimized structures are shown in Figs. S3 and S4. The results showed that full Li^+ substitution would reduce the cell volume in both LMO-types. In particular, the spinel-type LMO showed that full desorption of Li^+ from the 8a position (Table S3, structure $\text{H}_8\text{Li}_1\text{Mn}_{15}\text{O}_{32}$) involved a reduction

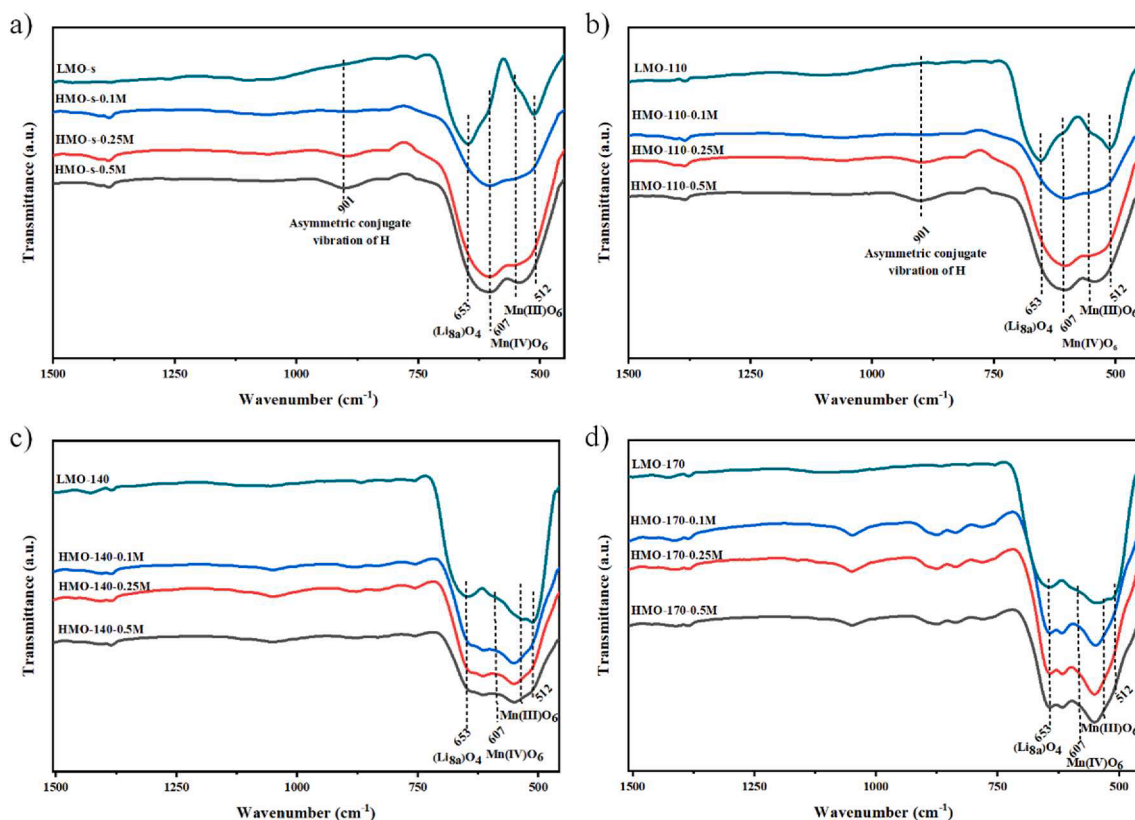


Fig. 7. FTIR spectra of the LMO nanocomposites after the acid treatment at different concentrations of HCl. HMO-s (a), HMO-110 (b), HMO-140 (c), and HMO-170 (d).

in cell volume greater than fully desorbed (Table S 3, structure $\text{H}_8\text{Mn}_{15}\text{O}_{32}$). On the other hand, the lattice parameters calculated for layered-type LMO evidenced that the cell volume was lower in substituting Li^+ atoms from $[\text{Li}^+]$ layers (see Table S4, structure $\text{H}_6\text{Li}_2\text{Mn}_4\text{O}_{12}$) than in the substitution of lithium atoms from the $[\text{LiMn}_2]$ layer (see Table S4, structure $\text{Li}_6\text{H}_2\text{Mn}_4\text{O}_{12}$). Similar results have been reported for simulations of the spinel-type LMO [33]. Table S5 compares the calculated lattice constants to the experimental lattice constants for spinel and layered type LMO. The calculated lattice parameters overestimate the experimental lattice parameter by approximately 2.3% for $\text{Li}_{1.12}\text{Mn}_{1.7}\text{O}_4$ and 0.2 to 0.7% for Li_2MnO_3 . Similar results were reported by other authors [33,59,60]. In this sense, to complement the study of the structural transformation of our materials, we carried out the simulation of XRD spectra for the different delithiated states of spinel and layered type LMO in pure phase (Fig. S5). Clearly, the characteristic (111) and (400) peaks for the spinel and (001) and (131) for the layered LMOs show slight shifts towards a higher 2θ angle, in agreement with what occurred in our experimental results. The (111), (311) and (400) diffraction peaks of the different delithiated states of spinel-type LMO were preserved (Fig. S5a). However, a slight shift in the (111) diffraction peak of the $\text{H}_8\text{Li}_1\text{Mn}_{15}\text{O}_{32}$ structure, corresponding to the substitution of Li^+ atoms from the 8a position, is observed. This shift is probably due to the reduction of the cell volume. No significant changes were found in the diffraction pattern of the $\text{Li}_8\text{H}_1\text{Mn}_{15}\text{O}_{32}$ structure corresponding to the substitution of Li^+ atoms from 16d position. On the other hand, the (001), (130), and (131) diffraction peaks for layered-LMO were preserved after gradual delithiation (Fig. S5b). Interestingly, the substitution of Li^+ atoms from the 2b position, corresponding to the transition metal layer, does not involve a substantial change with respect to the lithiated layered-type diffractogram. On the other side, the substitution of Li^+ atoms from the 2c and 4h positions, corresponding to the lithium layer, is similar to

the fully delithiated layered-type spectrum. Overall, our theoretical investigation showed that full Li^+ substitution would reduce the cell volume in both LMO-types. These results confirm the contraction of interplanar distance (table S6) and are in line with other studies [33]. Interestingly, the simulated XRD data suggest a structural transformation similar to what is observed experimentally in this work for delithiated LMO.

First-principles calculations were also used to provide insight into the electronic structure during the delithiation process of spinel and layered type LMO (Fig. 6). Fig. 6a-b shows the density of states (DOS) for the ground state structure of Li_2MnO_3 and its fully delithiated structure. Also, the DOS for the different delithiated structures of the layered LMO are shown in Fig. S6. In general, the density of states of the conduction band and the valence band of the lithiated and delithiated simulated materials are composed of O 2p and Mn 3d states. An overlap/hybridization between the 3d state of Mn and the 2p state of O (typical of 3d transition metal oxides) is observed in all simulations [60]. This observation indicates that the Mn–O bond exhibits covalent binding properties [61]. The occupied states close to the Fermi level are composed predominantly of O 2p states in all simulated structures. The bandgap decreased from 1.4 to 0.5 eV when the delithiation process occurred. It implies a change of the post-delithiation electronic properties in layered materials, becoming materials with a semi-metallic behavior. On the other hand, the DOS for the ground state structure of $\text{Li}_{1.12}\text{Mn}_{1.7}\text{O}_4$ and its fully delithiated structure is shown in Fig. 6c-d. Likewise, the DOS analysis for the different simulated delithiated structures is shown in Fig. 7S. The results evidenced that the electronic structure of $\text{Li}_{1.12}\text{Mn}_{1.7}\text{O}_4$ and their different delithiated state are governed by a strong hybridization between the O 2p and Mn 3d states. It is observed that all simulated structures have metallic electronic properties, such have been reported previously [62]. The Fermi level crosses the conduction band for the fully lithiated structure ($\text{Li}_9\text{Mn}_{16}\text{O}_{32}$), while for

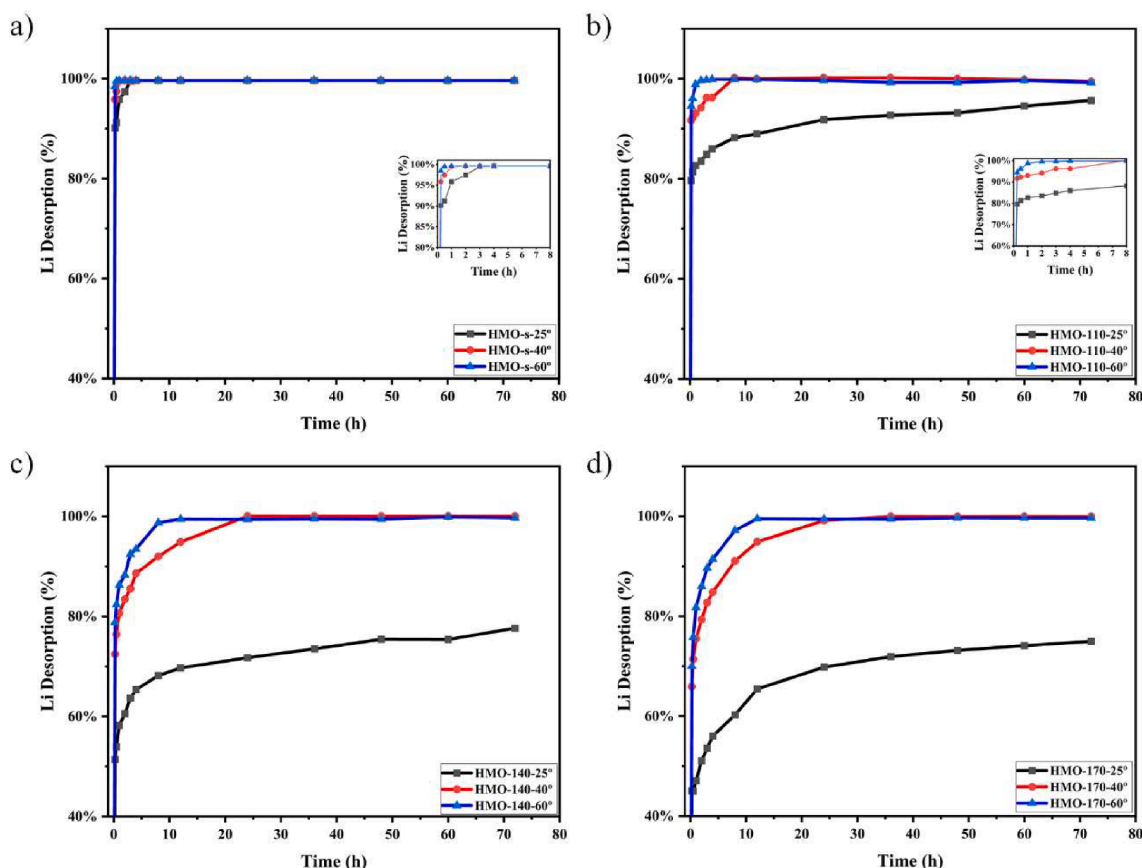


Fig. 8. Lithium desorption rate at different temperatures. LMO-s (a), LMO-110 (b), LMO-140 (c) and LMO-170 (d).

their different delithiated structures, the conduction band becomes filled. Comparable results have been reported in other studies [63].

FTIR was used as a complementary technique for browsing the near-neighbor environment of oxygen coordination around the lithium and manganese cations. Fig. 7 shows the FTIR spectra of LMO nanocomposites before and after the acid treatment (HMO samples). Two strong absorption bands characterize all LMO samples at around $500\text{--}700\text{ cm}^{-1}$. These bands are assigned to the asymmetric stretching vibrations of octahedral MnO_6 as a major contribution [64,65]. However, in this region, the stretching vibrations of the tetrahedral LiO_4 groups have also been reported around 650 cm^{-1} [33] and $350\text{--}550\text{ cm}^{-1}$ [66]. In this sense, infrared spectroscopy studies of lithium inorganic compounds have shown that at low and high frequency, the vibrations of MnO_6 groups are strongly coupled to LiO_n polyhedral vibrational modes (LiO_6 and LiO_4) [64]. In this regard, all samples presented a band at 653 cm^{-1} attributed to the vibration of the LiO_4 . Nevertheless, the increase of the Li_2MnO_3 layered phase in samples LMO-110, LMO-140, and LMO-170 gradually decreases the LiO_4 vibration band because this is an intrinsic band present in the spinel-type LMO [33]. Interestingly, the variation of the acid concentration has no significant effect on the FTIR spectra of the same samples series, which is consistent with previous results. However, a differential effect of the desorption process depending on the layer phase content was observed in the $500\text{--}700\text{ cm}^{-1}$ region. At high frequency, the vibrational mode assigned to LiO_4 (653 cm^{-1}) disappeared and the frequency coupled Mn (IV) O_6 octahedra vibrations decreased in the HMO-s and HMO-110 samples, evidencing that the desorption process takes place (Fig. 7a,b) [48]. In contrast, in the LMO-140 and LMO-170 samples with higher lithium content, the vibrational mode assigned to LiO_4 (653 cm^{-1}) weakened but not disappeared (Fig. 7c,d). Interestingly, at low frequency (Fig. S8), it was found that the vibrational mode corresponding to LiO_4 (around 422 cm^{-1}) disappeared in all samples. Nevertheless, the

vibrational modes assigned to LiO_6 ($250\text{--}350\text{ cm}^{-1}$ region) weakened but not disappeared. These results suggest that the desorption process is more favorable at LiO_4 tetrahedra than at LiO_6 octahedra. These results are consistent with the previous chemical analysis, which indicated that the percentage of lithium desorption is higher for the spinel-type nanocomposite (LMO-s and LMO-110) than for the layered-type nanocomposite (LMO-140 and LMO-170). Moreover, additional bands around $850\text{--}1050\text{ cm}^{-1}$ appear in all samples. These bands are attributed to the asymmetric conjugate vibration of H^+ supporting the occurrence ion-exchange process [34,48,67]. It is important to note, due to the above-mentioned stronger coupling between the LiO_n and MnO_n vibrational modes, the infrared spectrum of this type of material is complex. Then, further studies are necessary to elucidate the underlying nature of the vibrational modes of both LMO and their subsequent HMO materials.

3.3. Li^+ desorption process behavior at different temperatures

In order to understand in-depth and optimize the lithium desorption behavior of our nanocomposites, kinetic studies were carried out for up to 72 h at different temperatures (25, 40, and 60°C) with 0.1 M HCl solutions. Fig. 8 shows the effect of temperature on the lithium desorption process of the LMO nanocomposites. In general, all samples showed that the lithium desorption process was enhanced by increasing the temperature. Fig. 8a shows the kinetic behavior of the lithium desorption at different temperatures for the LMO-s sample. In this material, the lithium desorption is quickly completed within 8 h at 25°C . Similar results have been reported by Xiao *et al.*, for spinel-type LMO at room temperature [45]. However, after increasing the temperature to 40 and 60°C , the lithium desorption was fastly achieved at times 0.5 and 0.25 h, respectively, indicating the key role of the temperature in this process. In this sense, Gao *et al.*, reported that the lithium desorption

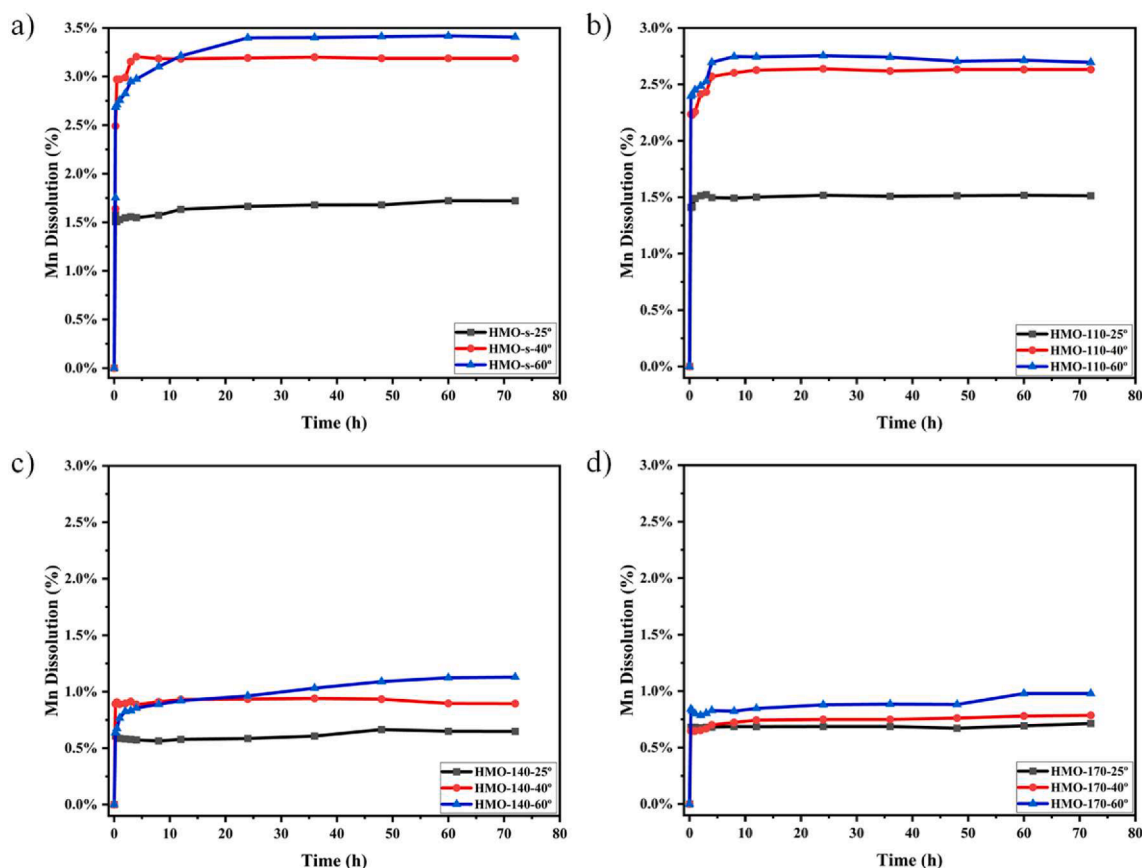


Fig. 9. Percentage of manganese dissolution at different temperatures. LMO-s (a), LMO-110 (b), LMO-140 (c) and LMO-170 (d).

rate increased rapidly when spinel-type LMO was submitted to 0.5 M HCl at 40 °C, reaching lithium desorption of 96.5% within 20 min [48]. Interestingly, our results show a temperature-dependent effect that is more evident when increasing the layered phases (Fig. 8b-d). In fact, at room temperature, the LMO-110, LMO-140, and LMO-170 do not achieve full lithium desorption. However, the increase in temperature accelerates the desorption process in all samples. Particularly in the HMO-110 sample, the lithium desorption process is full within 8 h at 40 °C and 4 h at 60 °C. HMO-140 and HMO-170 samples complete the process at 24 h and 12 h at 40 and 60 °C, respectively. In the context of layered metal oxide compounds, such as Li_2TiO_3 , it has been reported that for an increasing Li/Ti ratio (from 2.0 to 2.16), the lithium desorption decreases from 85.62% to 77.87% under the same desorption conditions (0.25 M HCl, 60 °C) [68]. A similar tendency is observed with the increase of the layered phase in our material. On the other hand, the increase in temperature increases the manganese dissolution in all samples (Fig. 9). Nevertheless, the spinel-type nanocomposites (Fig. 9 a-b) showed a higher percentage (1.7–3.4%) of manganese dissolution compared to lithium-rich nanocomposites (0.65–1.2%) (Fig. 9 c-d). It is important to mention that a higher manganese dissolution implies the destabilization of the crystalline structure of the LMOs, either layer or spinel, so it is a key parameter to be controlled [5,14,48].

Our results consistently indicate the existence of a dependence relation between the desorption behavior and the content of the layered type phase in the nanocomposite, being temperature, the driving force for the lithium desorption process. These results suggest that a study of the energetic profile and the lithium diffusion pathways is necessary. In this context, a thermochemical analysis of the Li^+/H^+ Exchange Energies based on DFT is included in the supporting information. The thermochemical analysis for the layered LMO shows that the Exchange Energy for the delithiation from the $[\text{LiMn}_2]$ layer is higher than from

the $[\text{Li}]$ layer. Additionally, a systematic study of the possible lithium diffusion pathways through first-principles nudged elastic band (NEB) calculations have been carried out. To describe the behavior of lithium diffusion in our materials, we studied the energy barrier of lithium diffusion to a nearby possible lithium vacancy. Fig. 10 shows the migration path energy barriers for Li diffusion between neighboring lithium sites in Li_2MnO_3 . Fig. 10a-b shows the two possible diffusion paths for the lithium atoms between the neighboring $[\text{Li}]$ and $[\text{LiMn}_2]$ layers in Li_2MnO_3 . The energy barriers of lithium diffusion from the 2b position of the $[\text{LiMn}_2]$ layer to the 2c and 4 h vacancy sites of the $[\text{Li}]$ layer were 0.8207 eV and 0.8214 eV, respectively. Fig. 10 c-e shows the three possible diffusion paths of the lithium atoms in the $[\text{Li}]$ layer. The energy barriers of Li at the 2c position of the $[\text{Li}]$ layer diffusing towards the 4 h vacancy site of the $[\text{Li}]$ layer was 1.0603 eV, while for the Li diffusion at the 4 h position of the $[\text{Li}]$ layer towards the 2c and 4 h vacancy sites of the $[\text{Li}]$ layer was 0.6840 and 1.0386 eV, respectively. These results suggest that the energy demand for the diffusion of the lithium atoms from the 2c position of the $[\text{Li}]$ layer to the 4 h vacancy site of the $[\text{Li}]$ layer is higher than other possible diffusion pathways in Li_2MnO_3 [29]. On the other hand, Fig. 11 shows the energy barriers of the possible lithium diffusion pathways for $\text{Li}_{1.12}\text{Mn}_{1.7}\text{O}_4$. Fig. 11a shows the diffusion of the lithium atom between the neighboring sites at position 8a. The energy barriers of Li at the 8a position diffusing into the vacancy of the 8a site was 0.2003 eV, while the energy barriers of Li at the 16d position diffusing into the vacancy of the 8a site was 1.1447 eV (Fig. 11b). This result agrees with the thermochemical analysis of the Li^+/H^+ Exchange Energies for the spinel LMO (Supporting information). Interestingly, it can be appreciated that there exists a significant difference in the energy barriers for the lithium diffusion between the spinel and the layered LMO. In fact, it suggests from the thermodynamical point of view that lithium desorption is easier to achieve in

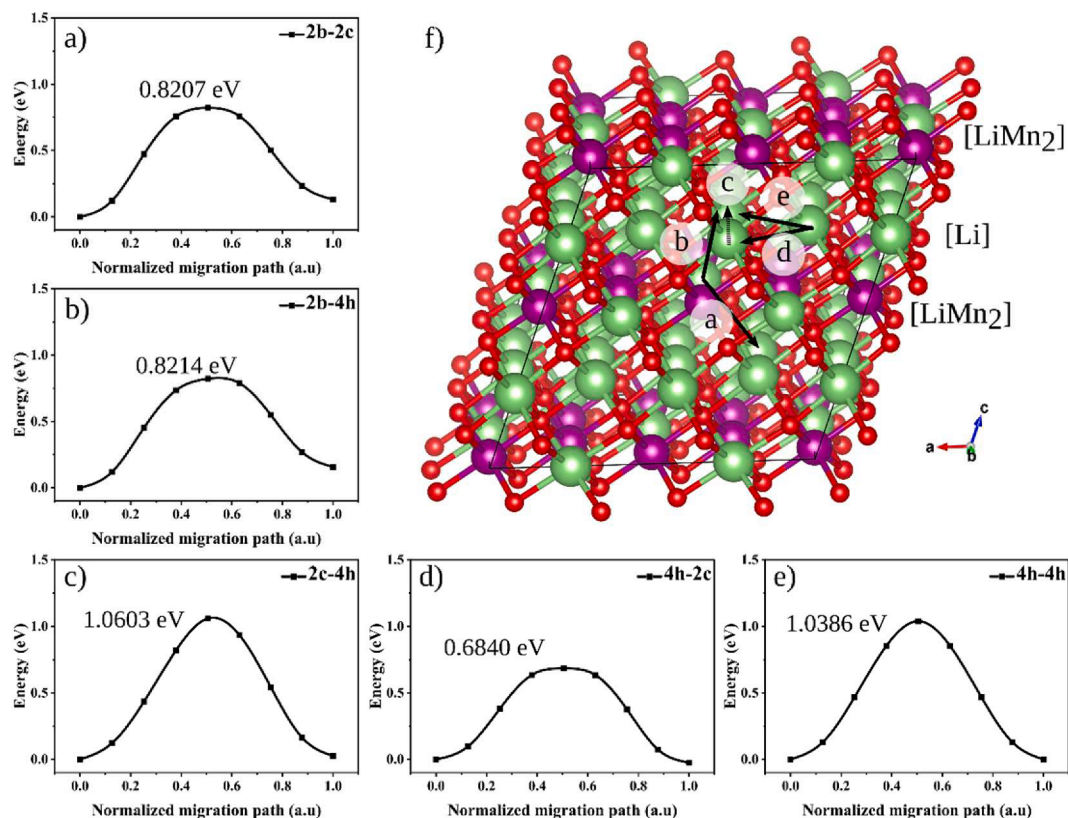


Fig. 10. Energy barriers of the Li diffusion inside Li_2MnO_3 supercell. Energy change of Li-ion moving from 2b to 2c (a), 2b to 4 h (b), 2c to 4 h (c), 4 h to 2c (d), 4 h to 4 h, and crystal structure illustration of the five typical hops between neighboring lithium sites (f).

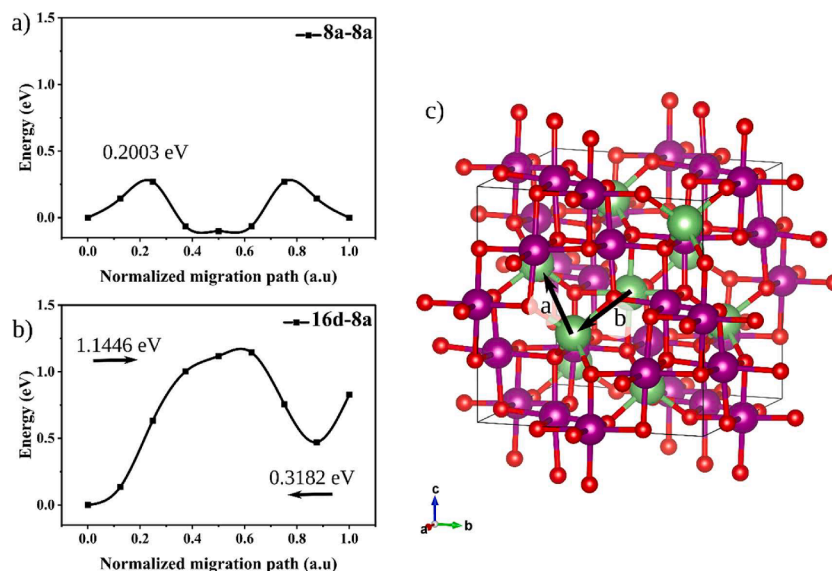


Fig. 11. Energy barriers of the Li diffusion LiMn_2O_4 . Energy change of Li ion moving from 8a to 8a (a), Energy change of Li ion moving from 16d to 8a (b) and crystal structure illustration of the two typical hops between neighboring lithium sites (c).

spinel than layered type LMO, which supports our experimental results.

In our study, HMO materials are obtained from the lithium-ion stripping from the crystalline lattice of the precursor materials (LMO) by acid treatment. This process involves forming hydrogenated states that act as lithium-ion sieves [21]. Thus, the HMO material is characterized by owning an active crystalline lattice that can intercalate/de-intercalated Li^+ or H^+ ions depending on the solution medium [14]. Because a critical aspect of LIS material proper function is the structure

stability [5,21,22], we analyzed the effect of the same acid treatment condition on the crystalline structure of the HMO of the most representative samples at low and high Li/Mn ratios by XRD. Fig. 12 compares the XRD spectra of spinel (a; LMO-s) and layered (b; LMO-170) LMO types and their resultant HMO after acid treatment at RT and 40 °C during 24 h. After the acid treatment, the main diffraction indices shifted to higher angles in spinel and layered LMO types. Fig. 12a shows that the increase in temperature from RT to 40 °C impacts the crystalline

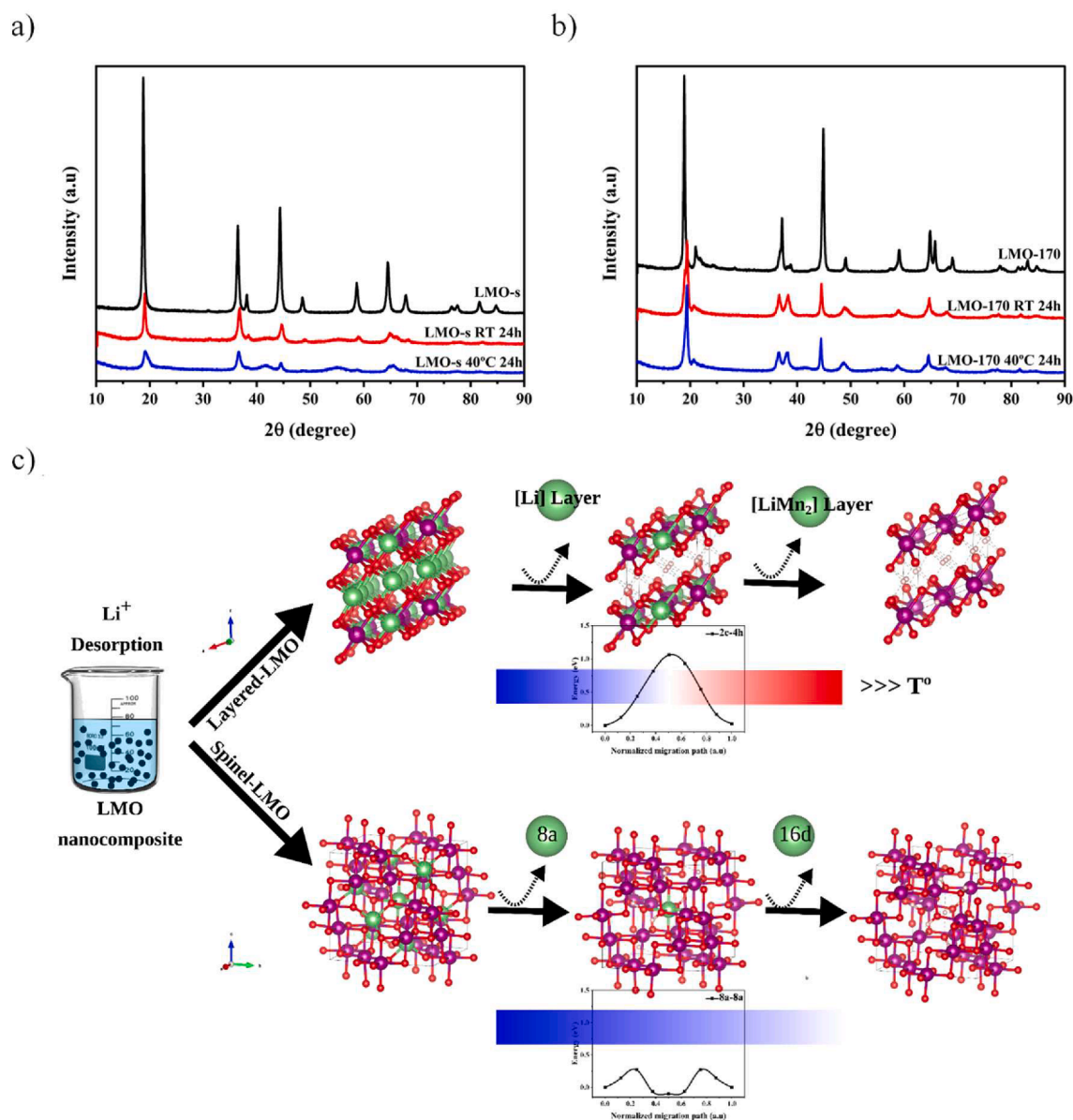


Fig. 12. Comparison of XRD spectra of spinel (a) and layered (b) LMO and their resultant HMO after acid treatment at RT and 40 °C during 24 h. Schematic picture of the LMO nanocomposite desorption behavior in HCl (c).

structure of the LMO-s sample, causing the formation of a quasi-amorphous structure at 40 °C. It seems clear that the loss of the crystal structure in spinel-type LMO can be, at least, be attributed to the increase in the Mn dissolution and further destabilization of the Mn-O framework at high temperatures. Our results closely match those obtained previously, suggesting that manganese dissolution affects the structural stability of the spinel LMO material [21,48,67].

On the contrary, an increase in the desorption temperature of LMO-170 favored the deintercalation of lithium from the crystal lattice of layered-type LMO (Fig. 12b), which is in line with the Li kinetic study. The main diffraction indices shifted even more to higher angles after acid treatment at 40 °C than RT. Interestingly, at 40 °C the crystalline structure of the LMO-170 is more preserved than the LMO-s. This result confirms the better stability of the Mn-O framework in the layered LMO than the spinel one, which is also evidenced in the Mn kinetic study. In fact, layered materials have been previously utilized to stabilize the crystalline structure of other materials in battery applications [69].

Altogether, these experimental and theoretical findings provide conclusive support indicating that lithium desorption by HCl is easier to

achieve in spinel than layered type LMO (Fig. 12c). Therefore, if these differences are not considered in the design of a desorption process for LMO nanocomposites, it could have negative consequences for the practical application of these materials. For instance, the destabilization of the crystal structure in spinel-type LMO and/or a reduced adsorption capacity in lithium-rich LMO due to unsuccessful Li desorption of the LIS material.

4. Conclusions

In the present study, we have investigated the lithium desorption behavior of different LMO nanocomposites in acidic media. LMO nanocomposites with different Li/Mn ratios were systematically formed by hydrothermal synthesis favoring the lithium-rich layered phase (Li₂MnO₃). Then, LMO nanocomposites and their delithiated products (HMO) were characterized in terms of crystal structure, morphology, size, and chemical composition. Herein, it is reported that there is a differential lithium desorption behavior that depends on the Li/Mn ratio of the nanocomposite. Using a computational approach assisted by DFT,

we have demonstrated that the diffusion energy barrier can explain these differences.

Interestingly, the experimental and simulated XRD spectra after lithium desorption process showed that the spinel-type LMOs maintain their crystalline structure, while both spinel and layered crystalline phases are detected in lithium-rich layered LMOs. In turn, a decrease in the cell volume and interplanar distance of the delithiated products was evidenced. Interestingly, DOS analysis shows that the fully delithiated materials exhibit the electrochemical properties of metallic materials. Remarkably, no significant effect of acid concentration on the desorption process was evidenced. FTIR showed that the desorption process strongly depends on the content of the layered-type LMO. Thus, the desorption of the tetrahedral LiO_4 groups is more favorable than that of the octahedral LiO_6 groups. On the other hand, the temperature was the driving force for a successful desorption process in lithium-rich materials. In this sense, the computational study of the different lithium diffusion routes by NEB showed that the differential desorption process found in our materials could be a consequence of the high energy barrier for lithium diffusion in layered-type LMO compared to spinel-type LMO. In this context, our investigation suggests that a detailed characterization of the starting material is necessary to choose a suitable desorption process. We are confident that this study will open up new approaches for the application of lithium-adsorbent materials based on lithium manganese oxide.

Declaration of Competing Interest

The authors declare that they have no known competing financial interests or personal relationships that could have appeared to influence the work reported in this paper.

Acknowledgements

We recognize to PhD. Programs in “Advanced Materials and Nanotechnologies” from Universidad Autónoma de Madrid (UAM, Spain) and “Ingeniería de Procesos de Minerales” from Universidad de Antofagasta (UA, Chile). This work was financially supported by CONICYT PFCHA/DOCTORADO/2015-21151648 (Ruth Pulido), PFCHA/DOCTORADO/2017-21172001 (Nelson Naveas) and partially funded by project USAMPSA, PID-2020-112770-C22, from the Government of Spain. The simulations used in this paper have been performed in the Centro de Computación Científica-Universidad Autónoma de Madrid (CCC-UAM); thanks to CPU time and other resources granted by the institution.

Appendix A. Supplementary data

Supplementary data to this article can be found online at <https://doi.org/10.1016/j.cej.2022.136019>.

References

- [1] H. Vikström, S. Davidsson, M. Höök, Lithium availability and future production outlooks, *Appl. Energy* 110 (2013) 252–266, <https://doi.org/10.1016/j.apenergy.2013.04.005>.
- [2] B. Swain, Recovery and recycling of lithium: A review, *Sep. Purif. Technol.* 172 (2017) 388–403, <https://doi.org/10.1016/j.seppur.2016.08.031>.
- [3] B.K. Pramanik, L.D. Nghiem, F.I. Hai, Extraction of strategically important elements from brines: constraints and opportunities, *Water Res.* 168 (2020), <https://doi.org/10.1016/j.watres.2019.115149>.
- [4] A. Karrech, M.R. Azadi, M. Elchalakani, M.A. Shahin, A.C. Seibi, A review on methods for liberating lithium from pegmatites, *Miner. Eng.* 145 (2020) 106085.
- [5] G. Liu, Z. Zhao, A. Ghahreman, Novel approaches for lithium extraction from salt-lake brines: a review, *Hydrometallurgy* 187 (2019) 81–100, <https://doi.org/10.1016/j.hydromet.2019.05.005>.
- [6] K. Ooi, A. Sonoda, Y. Makita, R. Chitrakar, Y. Tasaki-Handa, T. Nakazato, Recovery of lithium from salt-brine eluates by direct crystallization as lithium sulfate, *Hydrometallurgy* 174 (2017) 123–130, <https://doi.org/10.1016/j.hydromet.2017.10.007>.
- [7] P. Meshram, B.D. Pandey, T.R. Mankhand, Extraction of lithium from primary and secondary sources by pre-treatment, leaching and separation: A comprehensive review, *Hydrometallurgy* 150 (2014) 192–208, <https://doi.org/10.1016/j.hydromet.2014.10.012>.
- [8] G.A. Guter, G.S. Hammond, The separation of lithium from alkali metal ions 1,2, *J. Am. Chem. Soc.* 78 (1956) 5166–5167, <https://doi.org/10.1021/ja01601a009>.
- [9] L. Zhang, L. Li, H. Rui, D. Shi, X. Peng, L. Ji, X. Song, Lithium recovery from effluent of spent lithium battery recycling process using solvent extraction, *J. Hazard. Mater.* 398 (2020), 122840, <https://doi.org/10.1016/j.jhazmat.2020.122840>.
- [10] W. Xiang, S. Liang, Z. Zhou, W. Qin, W. Fei, Extraction of lithium from salt lake brine containing borate anion and high concentration of magnesium, *Hydrometallurgy* 166 (2016) 9–15, <https://doi.org/10.1016/j.hydromet.2016.08.005>.
- [11] A. Battistel, M.S. Palagonia, D. Brogioli, F. La Mantia, R. Trócoli, Electrochemical methods for lithium recovery: a comprehensive and critical review, *Adv. Mater.* 32 (2020) 1905440, <https://doi.org/10.1002/adma.201905440>.
- [12] W. Shi, X. Liu, C. Ye, X. Cao, C. Gao, J. Shen, Efficient lithium extraction by membrane capacitive deionization incorporated with monovalent selective cation exchange membrane, *Sep. Purif. Technol.* 210 (2019) 885–890, <https://doi.org/10.1016/j.seppur.2018.09.006>.
- [13] X. Liu, X. Chen, L. He, Z. Zhao, Study on extraction of lithium from salt lake brine by membrane electrolysis, *Desalination* 376 (2015) 35–40, <https://doi.org/10.1016/j.desal.2015.08.013>.
- [14] X. Xu, Y. Chen, P. Wan, K. Gasem, K. Wang, T. He, H. Adidharma, M. Fan, Extraction of lithium with functionalized lithium ion-sieves, *Prog. Mater. Sci.* 84 (2016) 276–313, <https://doi.org/10.1016/j.pmatsci.2016.09.004>.
- [15] Z. Zhao, X. Si, X. Liang, X. Liu, L. He, Electrochemical behavior of Li^+ , Mg^{2+} , Na^+ and K^+ in $\text{LiFePO}_4/\text{FePO}_4$ structures, *Trans. Nonferrous Met. Soc. China* 23 (2013) 1157–1164, [https://doi.org/10.1016/s1003-6326\(13\)62578-9](https://doi.org/10.1016/s1003-6326(13)62578-9).
- [16] Q.H. Zhang, S.P. Li, S.Y. Sun, X.S. Yin, J.G. Yu, LiMn_2O_4 spinel direct synthesis and lithium ion selective adsorption, *Chem. Eng. Sci.* 65 (2010) 169–173, <https://doi.org/10.1016/j.ces.2009.06.045>.
- [17] X.C. Shi, D.F. Zhou, Z.B. Zhang, L.L. Yu, H. Xu, B.Z. Chen, X.Y. Yang, Synthesis and properties of $\text{Li}_{1.6}\text{Mn}_{1.6}\text{O}_4$ and its adsorption application, *Hydrometallurgy* 110 (2011) 99–106, <https://doi.org/10.1016/j.hydromet.2011.09.004>.
- [18] D.-F. Liu, S.-Y. Sun, J.-G. Yu, A new high-efficiency process for Li^+ recovery from solutions based on $\text{LiMn}_2\text{O}_4/\lambda\text{-MnO}_2$ materials, *Chem. Eng. J.* 377 (2019), 119825, <https://doi.org/10.1016/j.cej.2018.08.211>.
- [19] A.-H. Marincas, F. Goga, S.-A. Dorneanu, P. Ilea, Review on synthesis methods to obtain LiMn_2O_4 -based cathode materials for Li-ion batteries, *J. Solid State Electrochem.* 24 (2020) 473–497, <https://doi.org/10.1007/s10008-019-04467-3>.
- [20] S. Safari, B.G. Lottermoser, D.S. Alessi, Metal oxide sorbents for the sustainable recovery of lithium from unconventional resources, *Appl. Mater. Today* 19 (2020), 100638, <https://doi.org/10.1016/j.apmt.2020.100638>.
- [21] D. Weng, H. Duan, Y. Hou, J. Huo, L. Chen, F. Zhang, J. Wang, Introduction of manganese based lithium-ion Sieve-a review, *Prog. Nat. Sci. Mater. Int.* 30 (2020) 139–152, <https://doi.org/10.1016/j.pnsc.2020.01.017>.
- [22] K. Shi, M. Luo, J. Ying, S. Zhen, Z. Xing, R. Chen, Extraction of lithium from single-crystalline lithium manganese oxide nanotubes using ammonium peroxodisulfate, *IScience* 23 (11) (2020) 101768.
- [23] F.R. Qian, M. Guo, Z.Q. Qian, Q. Li, Z.J. Wu, Z. Liu, Highly lithium adsorption capacities of $\text{H}_{1.6}\text{Mn}_{1.6}\text{O}_4$ ion-sieve by ordered array structure, *Chemistryselect.* 4 (2019) 10157–10163, <https://doi.org/10.1002/slct.201902173>.
- [24] R. Chitrakar, H. Kanoh, Y. Miyai, K. Ooi, A new type of manganese oxide (MnO_2 center dot $0.5\text{H}_2\text{O}$) derived from $\text{Li}_{1.6}\text{Mn}_{1.6}\text{O}_4$ and its lithium ion-sieve properties, *Chem. Mater.* 12 (2000) 3151–3157, <https://doi.org/10.1021/cm0000191>.
- [25] X.J. Yang, H. Kanoh, W.P. Tang, K. Ooi, Synthesis of $\text{Li}_{1.33}\text{Mn}_{1.67}\text{O}_4$ spinels with different morphologies and their ion adsorptivities after delithiation, *J. Mater. Chem.* 10 (2000) 1903–1909, <https://doi.org/10.1039/b000219o>.
- [26] J. Yao, L. Lv, C. Shen, P. Zhang, K.-F. Aguey-Zinsou, L. Wang, Nano-sized spinel LiMn_2O_4 powder fabricated via modified dynamic hydrothermal synthesis, *Ceram. Int.* 39 (2013) 3359–3364, <https://doi.org/10.1016/j.ceramint.2012.07.093>.
- [27] W.I.F. David, M.M. Thackeray, L.A. De Picciotto, J.B. Goodenough, Structure refinement of the spinel-related phases $\text{Li}_2\text{Mn}_2\text{O}_4$ and $\text{Li}_{0.2}\text{Mn}_2\text{O}_4$, *J. Solid State Chem.* 67 (1987) 316–323, [https://doi.org/10.1016/0022-4596\(87\)90369-0](https://doi.org/10.1016/0022-4596(87)90369-0).
- [28] D.H. Snyder, V.I. Hegde, M. Aykol, C. Wolverton, Computational discovery of Li-M-O ion exchange materials for lithium extraction from brines, *Chem. Mater.* 30 (2018) 6961–6968, <https://doi.org/10.1021/acs.chemmater.7b03509>.
- [29] R. Xiao, H. Li, L. Chen, Density functional investigation on Li_2MnO_3 , *Chem. Mater.* 24 (2012) 4242–4251, <https://doi.org/10.1021/cm3027219>.
- [30] Q. Yu, K. Sasaki, T. Hirajima, Bio-templated synthesis of lithium manganese oxide microtubes and their application in Li^+ recovery, *J. Hazard. Mater.* 262 (2013) 38–47, <https://doi.org/10.1016/j.jhazmat.2013.08.027>.
- [31] Q. Yu, E. Morioka, K. Sasaki, Characterization of lithium ion sieve derived from biogenic Mn oxide, *Microporous Mesoporous Mater.* 179 (2013) 122–127, <https://doi.org/10.1016/j.micromeso.2013.05.026>.
- [32] Q. Yu, K. Sasaki, In situ X-ray diffraction investigation of the evolution of a nanocrystalline lithium-ion sieve from biogenic manganese oxide, *Hydrometallurgy* 150 (2014) 253–258, <https://doi.org/10.1016/j.hydromet.2014.07.002>.
- [33] A. Gao, X. Hou, Z. Sun, S. Li, H. Li, J. Zhang, Lithium-desorption mechanism in LiMn_2O_4 , $\text{Li}_{1.33}\text{Mn}_{1.67}\text{O}_4$, and $\text{Li}_{1.6}\text{Mn}_{1.6}\text{O}_4$ according to precisely controlled acid treatment and density functional theory calculations, *J. Mater. Chem. A* 7 (2019) 20878–20890, <https://doi.org/10.1039/C9TA06080D>.
- [34] Q. Feng, Y. Miyai, H. Kanoh, K. Ooi, Li^+ extraction/insertion with spinel-type lithium manganese oxides – characterization of redox-type and ion-exchange-type sites, *Langmuir* 8 (1992) 1861–1867, <https://doi.org/10.1021/la00043a029>.

- [35] K. Sato, D.M. Poojary, A. Clearfield, M. Kohno, Y. Inoue, The surface structure of the proton-exchanged lithium manganese oxide spinels and their lithium-ion sieve properties, *J. Solid State Chem.* 131 (1997) 84–93, <https://doi.org/10.1006/jssc.1997.7348>.
- [36] S.Y. Sun, X.F. Song, Q.H. Zhang, J. Wang, J.G. Yu, Lithium extraction/insertion process on cubic Li-Mn-O precursors with different Li/Mn ratio and morphology, *Adsorpt. Int. Adsorpt. Soc.* 17 (2011) 881–887, <https://doi.org/10.1007/s10450-011-9356-0>.
- [37] R. Pulido, N. Naveas, T. Graber, R.J. Martin-Palma, F. Agulló-Rueda, I. Brito, C. Morales, L. Soriano, L. Pascual, C. Marini, J. Hernández-Montelongo, M. Manso Silván, Hydrothermal control of the lithium-rich Li_2MnO_3 phase in lithium manganese oxide nanocomposites and their application as precursors for lithium adsorbents, *Dalt. Trans.* 50 (2021) 10765–10778, <https://doi.org/10.1039/D1DT01638E>.
- [38] P. Giannozzi, O. Basergio, P. Bonfà, D. Brunato, R. Car, I. Carnimeo, C. Cavazzoni, S. de Gironcoli, P. Delugas, F. Ferrari Ruffino, A. Ferretti, N. Marzari, I. Timrov, A. Urru, S. Baroni, Quantum ESPRESSO toward the exascale, *J. Chem. Phys.* 152 (2020), 154105, <https://doi.org/10.1063/5.0005082>.
- [39] H.J. Monkhorst, J.D. Pack, Special points for Brillouin-zone integrations, *Phys. Rev. B* 13 (1976) 5188–5192, <https://doi.org/10.1103/PhysRevB.13.5188>.
- [40] K. Momma, F. Izumi, VESTA 3 for three-dimensional visualization of crystal, volumetric and morphology data, *J. Appl. Crystallogr.* 44 (2011) 1272–1276, <https://doi.org/10.1107/S0021889811038970>.
- [41] Vitalij K. Pecharsky, Peter Y. Zavalij, Solving Crystal Structure from Powder Diffraction Data, in: *Fundam. Powder Diffraction. Struct. Charact. Mater.*, Springer US, Boston, MA, 2009: pp. 497–545. doi: 10.1007/978-0-387-09579-0.15.
- [42] K. Shimoda, M. Oishi, T. Matsunaga, M. Murakami, K. Yamanaka, H. Arai, Y. Ukyo, Y. Uchimoto, T. Ohta, E. Matsubara, Z. Ogumi, Direct observation of layered-to-spinel phase transformation in Li_2MnO_3 and the spinel structure stabilised after the activation process, *J. Mater. Chem. A* 5 (2017) 6695–6707, <https://doi.org/10.1039/C6TA11151C>.
- [43] Y. Sun, H. Cong, L. Zan, Y. Zhang, Oxygen vacancies and stacking faults introduced by low-temperature reduction improve the electrochemical properties of Li_2MnO_3 nanobelts as lithium-ion battery cathodes, *ACS Appl. Mater. Interfaces* 9 (2017) 38545–38555, <https://doi.org/10.1021/acsami.7b12080>.
- [44] H. Park, N. Singhal, E.H. Jho, Lithium sorption properties of HMnO in seawater and wastewater, *Water Res.* 87 (2015) 320–327, <https://doi.org/10.1016/j.watres.2015.09.032>.
- [45] J.L. Xiao, X.Y. Nie, S.Y. Sun, X.F. Song, P. Li, J.G. Yu, Lithium ion adsorption-desorption properties on spinel $\text{Li}_4\text{Mn}_5\text{O}_{12}$ and pH-dependent ion-exchange model, *Adv. Powder Technol.* 26 (2015) 589–594, <https://doi.org/10.1016/j.appt.2015.01.008>.
- [46] F. Qian, B. Zhao, M. Guo, J. Li, Z. Liu, Z. Wu, K-gradient doping to stabilize the spinel structure of $\text{Li}_{1.6}\text{Mn}_{1.6}\text{O}_4$ for Li^+ recovery, *Dalt. Trans.* 49 (2020) 10939–10948, <https://doi.org/10.1039/D0DT02405H>.
- [47] F. Qian, B. Zhao, M. Guo, Z. Qian, N. Xu, Z. Wu, Z. Liu, Enhancing the Li^+ adsorption and anti-dissolution properties of $\text{Li}_{1.6}\text{Mn}_{1.6}\text{O}_4$ with Fe, Co doped, *Hydrometallurgy* 193 (2020), 105291, <https://doi.org/10.1016/j.hydromet.2020.105291>.
- [48] A. Gao, Z. Sun, S. Li, X. Hou, H. Li, Q. Wu, X. Xi, The mechanism of manganese dissolution on $\text{Li}_{1.6}\text{Mn}_{1.6}\text{O}_4$ ion sieves with HCl, *Dalt. Trans.* 47 (2018) 3864–3871, <https://doi.org/10.1039/C8DT00033F>.
- [49] W. Tang, X. Yang, K. Ooi, Formation and mechanism of plate-form manganese oxide by selective hydrothermal lithium extraction from monoclinic Li_2MnO_3 , in: *Hydrothermal React. Tech.*, World Scientific, 2003, pp. 41–49, https://doi.org/10.1142/9789812705228_0006.
- [50] W. Tang, H. Kanoh, X. Yang, K. Ooi, Preparation of plate-form manganese oxide by selective lithium extraction from monoclinic Li_2MnO_3 under hydrothermal conditions, *Chem. Mater.* 12 (2000) 3271–3279, <https://doi.org/10.1021/cm000360l>.
- [51] L. Wang, W. Ma, R. Liu, H.Y. Li, C.G. Meng, Correlation between Li^+ adsorption capacity and the preparation conditions of spinel lithium manganese precursor, *Solid State Ionics* 177 (2006) 1421–1428, <https://doi.org/10.1016/j.ssi.2006.07.019>.
- [52] L. Zhang, D. Zhou, G. He, F. Wang, J. Zhou, Effect of crystal phases of titanium dioxide on adsorption performance of H_2TiO_3 -lithium adsorbent, *Mater. Lett.* 135 (2014) 206–209, <https://doi.org/10.1016/j.matlet.2014.07.176>.
- [53] S.F. Amalraj, L. Burlaka, C.M. Julien, A. Mauger, D. Kovacheva, M. Talianker, B. Markovsky, D. Aurbach, Phase transitions in Li_2MnO_3 electrodes at various states-of-charge, *Electrochim. Acta* 123 (2014) 395–404, <https://doi.org/10.1016/j.jelectacta.2014.01.051>.
- [54] S. Han, Y. Xia, Z. Wei, B. Qiu, L. Pan, Q. Gu, Z. Liu, Z. Guo, A comparative study on the oxidation state of lattice oxygen among $\text{Li}_{1.14}\text{Ni}_{0.136}\text{Co}_{0.136}\text{Mn}_{0.544}\text{O}_2$, Li_2MnO_3 , $\text{LiNi}_{0.5}\text{Co}_{0.2}\text{Mn}_{0.3}\text{O}_2$ and LiCoO_2 for the initial charge-discharge, *J. Mater. Chem. A* 3 (2015) 11930–11939, <https://doi.org/10.1039/C5TA02161H>.
- [55] M. Cheng, W. Tang, Y. Sun, K. Zhu, Electrochemical properties of Li_2MnO_3 nanocrystals synthesized using a hydrothermal method, *RSC Adv.* 5 (2015) 71088–71094, <https://doi.org/10.1039/C5RA08387G>.
- [56] R. Saroha, A. Gupta, A.K. Panwar, Electrochemical performances of Li-rich layered-layered Li_2MnO_3 - LiMnO_2 solid solutions as cathode material for lithium-ion batteries, *J. Alloy. Compd.* 696 (2017) 580–589, <https://doi.org/10.1016/j.jallcom.2016.11.199>.
- [57] R. Chitrakar, Y. Makita, K. Ooi, A. Sonoda, Lithium recovery from salt lake brine by H_2TiO_3 , *Dalt. Trans.* 43 (2014) 8933–8939, <https://doi.org/10.1039/c4dt00467a>.
- [58] C.L. Yu, F. Wang, S.Y. Cao, D.P. Gao, H.B. Hui, Y.Y. Guo, D.Y. Wang, The structure of H_2TiO_3 -a short discussion on “Lithium recovery from salt lake brine by H_2TiO_3 ”, *Dalt. Trans.* 44 (2015) 15721–15724, <https://doi.org/10.1039/c4dt03689a>.
- [59] B. Xu, S. Meng, Factors affecting Li mobility in spinel LiMn_2O_4 —A first-principles study by GGA and GGA+U methods, *J. Power Sources* 195 (2010) 4971–4976, <https://doi.org/10.1016/j.jpowsour.2010.02.060>.
- [60] H. Chen, M.S. Islam, Lithium extraction mechanism in Li-Rich Li_2MnO_3 involving oxygen hole formation and dimerization, *Chem. Mater.* 28 (2016) 6656–6663, <https://doi.org/10.1021/acs.chemmater.6b02870>.
- [61] H. Zhang, X. Du, S. Ding, Q. Wang, L. Chang, X. Ma, X. Hao, C. Pen, DFT calculations of the synergistic effect of λ - MnO_2 /graphene composites for electrochemical adsorption of lithium ions, *PCCP* 21 (2019) 8133–8140, <https://doi.org/10.1039/C9CP00714H>.
- [62] S. Bağcı, H.M. Tütüncü, S. Duman, E. Bulut, M. Özcar, G.P. Srivastava, Physical properties of the cubic spinel LiMn_2O_4 , *J. Phys. Chem. Solids* 75 (2014) 463–469, <https://doi.org/10.1016/j.jpcs.2013.12.005>.
- [63] C.Y. Ouyang, S.Q. Shi, M.S. Lei, Jahn-Teller distortion and electronic structure of LiMn_2O_4 , *J. Alloy. Compd.* 474 (2009) 370–374, <https://doi.org/10.1016/j.jallcom.2008.06.123>.
- [64] C. Julien, Local Environment in 4-Volt Cathode Materials for Li-Ion Batteries, in: 2000: pp. 309–326. doi: 10.1007/978-94-011-4333-2.13.
- [65] C.M. Julien, Local structure of lithiated manganese oxides, *Solid State Ionics* 177 (2006) 11–19, <https://doi.org/10.1016/j.ssi.2005.10.012>.
- [66] C. Julien, M. Massot, Structural transitions in positive electrodes for Li-ion batteries the vibronic approach, *Ionics (Kiel)* 8 (2002) 6–16, <https://doi.org/10.1007/BF02377748>.
- [67] Z.Y. Ji, M.Y. Zhao, J.S. Yuan, J. Wang, J.Q. Zhou, H.B. Yin, B.Y. Sun, Li^+ extraction from spinel-type LiMn_2O_4 in different eluents and Li^+ insertion in the aqueous phase, *Solvent Extr. Ion Exch.* 34 (2016) 549–557, <https://doi.org/10.1080/07366299.2016.1221266>.
- [68] X. Shi, Z. Zhang, D. Zhou, L. Zhang, B. Chen, L. Yu, Synthesis of Li^+ adsorbent (H_2TiO_3) and its adsorption properties, *Trans. Nonferrous Met. Soc. China* 23 (2013) 253–259, [https://doi.org/10.1016/S1003-6326\(13\)62453-X](https://doi.org/10.1016/S1003-6326(13)62453-X).
- [69] R.C. Longo, C. Liang, F. Kong, K. Cho, Core-shell nanocomposites for improving the structural stability of Li-rich layered oxide cathode materials for Li-ion batteries, *ACS Appl. Mater. Interfaces* 10 (2018) 19226–19234, <https://doi.org/10.1021/acsami.8b03898>.